OPEN

Light: Science & Applications (2017) 6, e17060; doi:10.1038/lsa.2017.60
Official journal of the CIOMP 2047-7538/17
www.nature.com/lsa

ORIGINAL ARTICLE

Enhanced second-harmonic generation from two-dimensional $MoSe_2$ on a silicon waveguide

Haitao Chen[1], Vincent Corboliou[1,2], Alexander S Solntsev[1], Duk-Yong Choi[3], Maria A Vincenti[4], Domenico de Ceglia[4], Costantino de Angelis[5], Yuerui Lu[6] and Dragomir N Neshev[1]

Two-dimensional transition-metal dichalcogenides (TMDCs) with intrinsically broken crystal inversion symmetry and large second-order nonlinear responses have shown great promise for future nonlinear light sources. However, the sub-nanometer monolayer thickness of such materials limits the length of their nonlinear interaction with light. Here, we experimentally demonstrate the enhancement of the second-harmonic generation from monolayer $MoSe_2$ by its integration onto a 220-nm-thick silicon waveguide. Such on-chip integration allows for a marked increase in the interaction length between the $MoSe_2$ and the waveguide mode, further enabling phase matching of the nonlinear process. The demonstrated TMDC–silicon photonic hybrid integration opens the door to second-order nonlinear effects within the silicon photonic platform, including efficient frequency conversion, parametric amplification and the generation of entangled photon pairs.
Light: Science & Applications (2017) **6,** e17060; doi:10.1038/lsa.2017.60; published online 20 October 2017

Keywords: 2D material; $MoSe_2$; SHG; waveguide

INTRODUCTION

Monolayers of transition-metal dichalcogenides (TMDCs), such as $MoSe_2$, exhibit unique optoelectronic properties, which include (but are not limited to) direct bandgap, robust valley polarization and strong electric tunability. These properties have opened opportunities for a number of applications, including 'flat-land' emitters[1–3] and valley-based applications[4–7]. Recently, the nonlinear optical wavelength conversion of two-dimensional (2D) TMDCs and, in particular, second-harmonic generation (SHG) have attracted significant attention[8–23], as these 2D materials are intrinsically non-centrosymmetric. Extraordinarily strong SHG has been reported for various materials such as monolayer MoS_2 (Refs 8,11,16), $MoSe_2$ (Ref. 13) and WS_2 (Ref. 15). Second-harmonic (SH) microscopy has also become a reliable tool to determine crystal properties and orientation[8,10,17,18]. In addition, recent findings have shown that the SHG from 2D materials could be markedly enhanced by resonant pumping[19] and controlled through electrical gating[20]. However, in all experiments to date, the 2D materials are excited along the normal of the monolayer, and the overall nonlinear conversion efficiency is limited by the sub-nanometer length of the nonlinear interaction with light, thus preventing their future practical application. Although optomechanical platforms[14,21] and micro-cavities[22,23] have been proposed or used to enhance the SHG from 2D materials, these approaches either are not compatible with the widely used silicon-based platform or require complex fabrication and positioning skills.

On the other hand, silicon photonics has a crucial role in modern photonic technologies, including a number of nonlinear applications for frequency conversion and signal processing. However, the centrosymmetric properties of silicon inhibit any second-order (or $\chi^{(2)}$) nonlinear effects, such as SHG, thus limiting a range of possible applications[24–26]. Various hybrid integration approaches for incorporating non-centrosymmetric materials in the silicon photonics platform have been suggested[27] to achieve second-order nonlinearity[25], however with very limited success. The 2D TMDCs can likely provide a viable solution for integration within the silicon photonics platform because of their strong van der Waals interactions with surfaces. Furthermore, because of their ultrathin nature, the integration with Si waveguides will not disturb the waveguide modes[28] or hinder other functionalities. However, the integration of 2D TMDCs with Si waveguides and the demonstration of second-order nonlinear effects, such as SHG, have not been demonstrated to date.

Here, we develop a monolayer $MoSe_2$ Si-waveguide integrated, scalable platform for second-order nonlinear effects in silicon photonics, and experimentally demonstrate strong SHG enhancement in comparison with free-space SHG from TMDCs. Importantly, our experiments show that the length of the nonlinear interaction with light for 2D TMDCs could be markedly increased through integration

[1]Nonlinear Physics Centre, Research School of Physics and Engineering, Australian National University, Canberra, ACT 2601, Australia; [2]Institut d'Optique Graduate School, Université Paris-Sud, Palaiseau 91127, France; [3]Laser Physics Centre, Research School of Physics and Engineering, Australian National University, Canberra, ACT 2601, Australia; [4]National Research Council, Charles M. Bowden Laboratory, Redstone Arsenal, Valhermoso Springs, AL 35898-5000, USA; [5]Department of Information Engineering and INO CNR, University of Brescia, Via Branze 38, Brescia 25123, Italy and [6]Research School of Engineering, College of Engineering and Computer Science, Australian National University, Canberra, ACT 2601, Australia
Correspondence: DN Neshev, Email: Dragomir.Neshev@anu.edu.au
Received 5 January 2017; revised 28 March 2017; accepted 29 March 2017; accepted article preview online 31 March 2017

with waveguides and can even achieve exact phase matching of $\chi^{(2)}$ parametric processes in a silicon photonics platform. Our results pave the way for practical $\chi^{(2)}$ nonlinear applications in silicon, including efficient wavelength conversion, parametric amplification and the generation of entangled photons.

MATERIALS AND METHODS

A 220-nm layer of hydrogenated amorphous silicon was deposited onto a SiO_2/Si wafer by plasma-enhanced vapor deposition at 300 °C, and the refractive index and extinction coefficient of the material was subsequently measured using ellipsometry methods. Then, the grating structure was patterned by electron beam lithography at 20 kV using positive resist ZEP-520A from Zeon Chemicals, Tokyo, Japan. The development was performed by inserting the sample into *n*-Amyl acetate. The resultant resist pattern was used as an etch mask for amorphous silicon etching in CHF_3/SF_6 plasma. The residual resist was removed by oxygen plasma. Subsequently, a single layer of $MoSe_2$ sample was mechanically exfoliated from the bulk crystal and drily transferred onto the sample.

For SHG measurements, a FemtoFiber Pro IR femtosecond laser (Toptica, Gräfelfing, Germany) with a central wavelength of 1550 nm, a repetition rate of 80 MHz and a pulse duration of 82 fs was used to pump the sample. Unless otherwise specified, an average power of 20 mW was used. An in-house microscopy system with a 20× objective was used for excitation and collection. The focused laser spot size was ~ 5 μm, and the peak power density was ~ 15 GW cm^{-2}. In the polarization resolved measurements, a half-waveplate was used to rotate the incident light polarization, and another polarizer was used for detection.

The micro-photoluminescence (PL) spectroscopy and micro-PL spatial mapping were performed on a commercial WiTec alpha300S system (Ulm, Germany) in the confocal microscope configuration, at an excitation of 532 nm using a continuous-wave laser.

RESULTS AND DISCUSSION

The concept behind the integration of $MoSe_2$ on a Si waveguide is illustrated in Figure 1a (side view). A grating inscribed onto the waveguide is used to couple light from free space into the waveguide. The evanescent field of the waveguide mode at the fundamental frequency (FF) of ~ 1550 nm overlaps with the $MoSe_2$ material on top of the waveguide to generate SH wave. The generated SH can be guided and extracted out of the waveguide into the free space by another grating coupler. Importantly, this scheme can also promote other $\chi^{(2)}$ nonlinear processes, including parametric amplification and spontaneous parametric down conversion (SPDC).

A slab waveguide was used in our experiments because it allows us to test the SHG at different propagation directions with respect to the TMDC crystalline orientation. Compared with crystalline silicon, whose absorption starts to increase sharply below 1100 nm, hydrogenated amorphous silicon is transparent up to 700 nm owing to the high optical bandgap of 1.73 eV[29]. Hence, the amorphous silicon was chosen in this work because of its low optical loss at both spectral regions around 1550 nm (FF) and 775 nm (SH). The thickness of 220 nm was chosen because it has been commonly used for silicon photonics platforms[30,31]. Furthermore, as shown in Supplementary Fig. S1a, the TE_0 mode of the FF exhibits a relatively strong evanescent field on the surface of the waveguide.

To design the grating couplers for the FF and the SH fields, we computed both the effective refractive indices of the TE_0 mode for FF and TE_1 mode for SH. For simplicity, we used a conventional binary grating design based on the calculated results, as schematically shown in Figure 1b (upper panel). In addition, a scanning electron micrograph (SEM) of the top view of the grating is shown in Figure 1b (lower panel). In general, the coupling efficiency of the grating depends on several parameters, including the incident beam profile, incident angle, grating geometry, grating period, duty cycle and etching depth[32]. In our work, but without loss of generality, we implemented a grating with a 50% duty cycle and a period that enabled the in/out-coupling at normal incidence for the first diffraction order[32]. We experimentally tested a set of etching depths and achieved a coupling efficiency of ~ 16% that was reasonably good for our purpose and comparable to other couplers reported in the literature[33,34]. To enable multiple angles of excitation with respect to the $MoSe_2$ crystal and to achieve optimal coupling into the waveguide, we used a circular geometry for the grating coupler[35], where one-half of the grating was designed for in-coupling of light at a wavelength of 1550 nm, whereas the other half out-coupled light at 775 nm. The optical image of the top view of the grating is shown in Figure 1c (left panel).

Next, a monolayer of $MoSe_2$ was exfoliated from a bulk crystal and drily transferred onto the planar waveguide area inside the circular grating. Because the optical contrast between the monolayer and the amorphous silicon is relatively poor, we used PL mapping instead of optical microscopy to locate the $MoSe_2$ position. Figure 1c (right panel) shows the 2D PL mapping image of the sample: the monolayer $MoSe_2$ crystal is the bright piece inside the grating circle. To confirm that the transferred piece was indeed a monolayer, we measured its PL emission spectrum. Figure 1d shows the PL spectrum from the location marked with a blue dot, as indicated in Figure 1c (right panel). The spectral peak is ~ 1.6 eV that agrees well with previous reports[36–38].

In the next step, we studied the SHG from the $MoSe_2$ monolayer. As discussed previously, the process of SHG is strongly enhanced by resonant pumping, near the two-photon transition[19]. This justifies our material choice of $MoSe_2$, whose exciton transition is resonantly matched to the two-photon energy of our pump laser (~0.8 eV). Under excitation by the focused FF beam, we observed strong exciton emission at 1.6 eV. The grating size in the radial direction of our sample was 10 μm, and the focused laser spot was ~ 5 μm; hence, we could choose to focus the laser spot either directly on the monolayer $MoSe_2$ or on the grating area. Figure 2a shows the spectra (normalized to the maximum value) collected from the sample when exciting the $MoSe_2$ crystal directly from free space (blue spot in Figure 1c) and from the waveguide through the grating coupler (red spot in Figure 1c). Here, the spectral signal only comes from the monolayer $MoSe_2$, as we did not observe any measurable signal from the waveguide region without $MoSe_2$ using a separate reference sample. Importantly, we observed approximately five times enhancement of the emission signal at 1.6 eV when exciting the monolayer by the evanescent waveguide mode, as compared to excitation from free space. We found that the signal intensity did not depend on the pump-laser polarization when focusing on the $MoSe_2$ directly from free space. However, when focusing on the grating, the signal intensity was heavily dependent on pump-laser polarization, as expected for the properties of our grating coupler. The spectral data shown here were collected by optimizing the polarization for the red spot, which corresponded to the position with a nearly maximum interaction length in our system.

Because the pump-laser was in resonance with the exciton energy, the SH emission and two-photon luminescence (2P-PL) were nearly degenerate. However, we still observed two peaks when focusing the laser on $MoSe_2$ directly (R1 and R2 in Figure 2a). There was also a

 doi:10.1038/lsa.2017.60

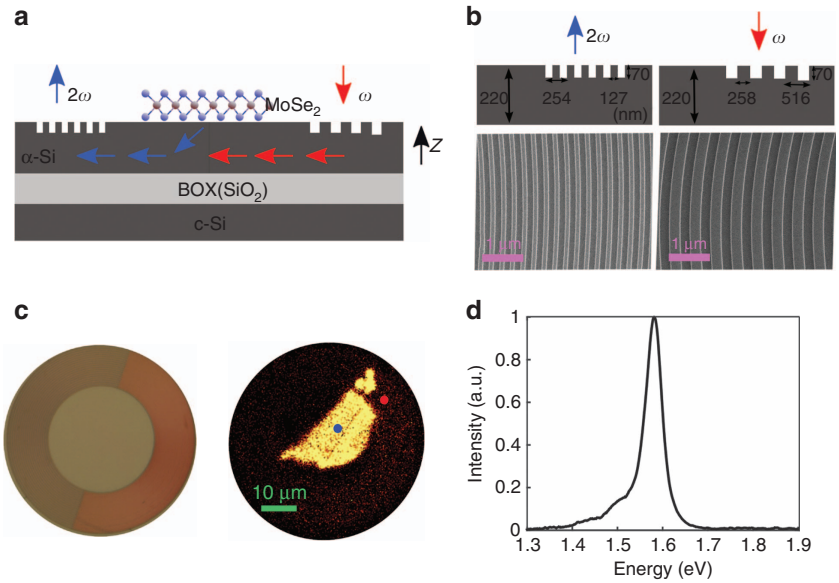

Figure 1 Linear characterization. (**a**) Schematic design of the hybrid integration of $MoSe_2$ onto a Si-waveguide. (**b**) top: Schematic side view of the grating coupler for both in- and out-coupling, where the numbers mark the physical dimensions in nm; bottom: SEM top view of the two grating couplers. (**c**) Optical image of the sample before transferring the $MoSe_2$ monolayer (left), PL mapping of the sample after $MoSe_2$ transfer (right), the bright area corresponds to the $MoSe_2$ monolayer. (**d**) PL spectrum of the monolayer $MoSe_2$ at room temperature, measured on the blue spot in **c**. In **c** and **d**, the PL is excited by a 532-nm laser.

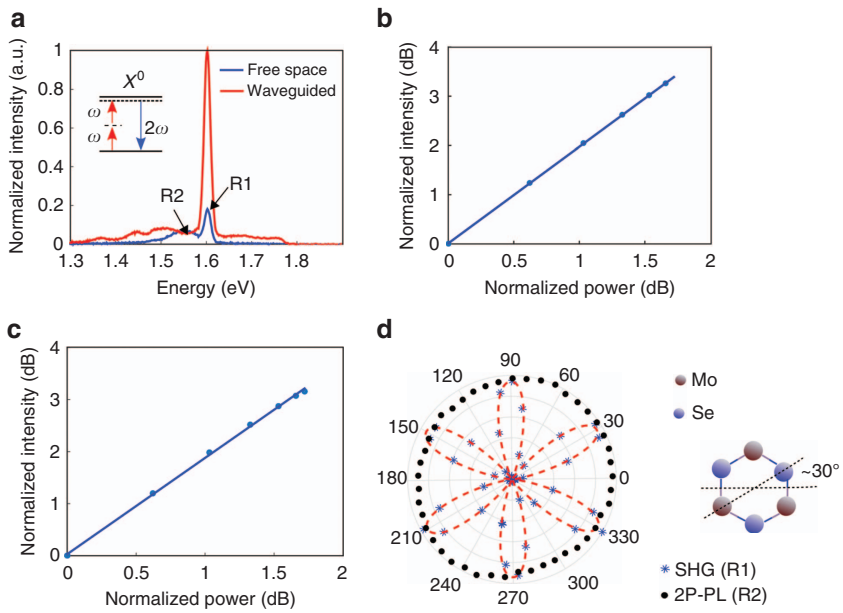

Figure 2 Nonlinear SHG microscopy. (**a**) Emission spectra measured from the sample when focusing the pump laser on the grating (red) and on the $MoSe_2$ (blue). The focusing positions are shown as red and blue spots, respectively, in Figure 1c. (**b**, **c**) Power dependence (in a log-log scale) of peaks R1 (**b**) and R2 (**c**), as indicated in **a**. The values are normalized to the quantities obtained at 2.9 mW of FF power. The dots are the measured data, and the line shows the expected quadratic dependence. (**d**) The polar intensity distribution of the emission component polarized parallel to the FF pump, when rotating the pump-laser polarization, φ, by 360° for both the SH signal (asterisk and red dashed fitting line) and 2P-PL (black dots). The 30°–210° direction corresponds to the armchair axis of the monolayer $MoSe_2$, shown schematically on the right-hand side.

broad tail in the emission spectrum when focusing on the grating, which is likely caused by the fact that the laser we used in our experiments was relatively broadband (from 0.79 to 0.81 eV, as shown in Supplementary Fig. S1b). Although the signal-R1 dominated the emission, we found that both peaks scaled quadratically with the excitation power, as shown in Figure 2b and 2c, respectively. To further distinguish them, we measured how the different emission components depend on the polarization of the pump laser coupled from free space. Figure 2d shows the polar distribution of the emission intensity parallel to the incident laser polarization (co-polarized component) as a function of the polarization of the excitation laser. We observed a sixfold pattern for the main peak R1 (asterisk and red dashed line), which is expected for the SH signal in a TMDC monolayer[8,10,11,17,18] and reflects the 3-fold rotational symmetry of

the crystal. From these SH microscopy measurements, we also determined the crystalline orientation of the $MoSe_2$ monolayer. This is schematically depicted on the right side of Figure 2d. By contrast, the intensity of the co-polarized component of peak R2, shown as black dots in Figure 2d, did not depend on the pump-laser polarization. These polarization measurements confirm that the resonant peak R1 is indeed the SH signal, whereas the other peaks with a much weaker intensity are 2P-PL. In the following discussion, we will focus only on the SH signal.

As mentioned above, the grating coupler is sensitive to the incident laser polarization and works best for TE_0-mode coupling, namely, when the laser is polarized along the tangential direction of the circular grating. The case of 2D material on top of a waveguide under TE_0 excitation was first studied theoretically by Haus and Reider some 30 years ago[39], and recent predictions[40] have shown that such geometry can lead to strong SHG enhancement. However, no experimental testing of these ideas has been attempted to date. Here, we measured the SH signal as a resulting from such interaction. To demonstrate in detail, two typical points P1 and P2 were excited on the grating, as shown in Figure 3a (left panel). The coordinate system is the same as in Figure 2d. P2 is on the armchair axis, and P1 is at an angle of ~30° to it. Figure 3a (right panel) shows the positions of P1 and P2 relative to the coordinate system and $MoSe_2$ orientation. Firstly, we measured the overall SH intensity dependence on the polarization of the pump laser over 360°, as shown in Figure 3b (i, ii) for P1 and P2, respectively. The coordinate system is the same as in Figure 3a, and the angle corresponds to the polarization of the pump laser. We could see from these two images that both dependencies display a figure-of-eight shape distribution. This shape is entirely defined by the coupling characteristic of the grating, as the in-coupling is efficient only for one polarization.

However, the polarization dependence changes when we measure the co-polarized component of SH to the pump laser, when varying the pump-laser polarization. The results are shown in Figure 3b (iii, iv) for P1 and P2 excitation, respectively. We observed different profiles for these two positions, which is likely due to the combined effects from the grating coupler and the 3-fold rotational symmetry of the monolayer $MoSe_2$. Furthermore, we took snapshots of the emission when pumping at these two points, as shown in Figure 3c. Bandpass filters have been applied to ensure that the signal captured by the camera is dominated by the SH signal. We could see that the SH signal was generated at the position of the $MoSe_2$ monolayer and was guided into the waveguide, being subsequently coupled out from the grating on the left. We noted that some emission also came out from the input end and some signal was scattered out directly from the material into free space. Importantly, the out-coupling signal was stronger when pumping from P1 compared with P2. On the basis of these results, we could see some hints that phase matching between the TE_0 mode for pumping and the TE_1 mode for SHG had a role here; however, the findings also indicated that multiple nonlinear wave-mixing processes existed in our system.

To support our experimental results and explore further directions to optimize our system, we performed simulations based on coupled-mode theory[41]. The intensity of the SH signal depends on several factors, namely, the overlap integral between the FF and SH guided modes, the phase matching between these modes, the crystal orientation defined by the guided-mode wave vector and the armchair direction of the $MoSe_2$ crystal, the efficiency of the input grating for the pump-laser beam and the efficiency of the output grating in the extraction of SH light. In Figure 4a, we plotted the effective mode index as a function of the waveguide thickness for the guided modes involved in the SHG, assuming 1550 nm as the pump-laser wavelength.

The waveguide supports three phase-matching points for SHG (red circles in Figure 4a), involving three different combinations of guided modes at the FF and SH frequencies. The silicon core thickness (220 nm) is close to two of these points: one is associated with the $TE_0 \rightarrow TE_1$ SHG process, whereas the other is related to the $TM_0 \rightarrow TM_1$ process. Our simulations suggest that the structure of the input grating, which mainly couples FF light into the TE_0 guided mode, favors the $TE_0 \rightarrow TE_1$ interaction. In addition to this process, the nonlinear monolayer allows two other interactions originated from the FF TE_0 mode, that is, the $TE_0 \rightarrow TM_0$ and the $TE_0 \rightarrow TM_1$. This shows the flexibility of our hybrid-integration scheme for selecting different parametric interactions, including other three wave-mixing

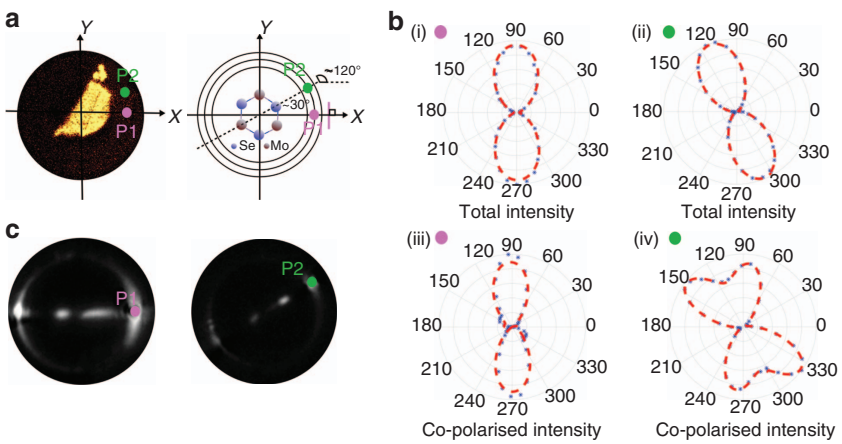

Figure 3 SHG from the $MoSe_2$-loaded Si waveguide. (**a**) Map of the sample orientation relative to the polar coordinate system for the measured sample (left) and schematic view (right); the armchair of the $MoSe_2$ is ~30° to the horizontal axis. The two spots P1 and P2 are the different positions of the laser focus on the grating, when exciting the waveguide mode. (**b**) Total SH emission intensity dependence on the pump-laser polarization, when focusing on position P1 (i) and P2 (ii), respectively. Co-polarized component of the SH intensity dependence on pump-laser polarization for P1 (iii) and P2 (iv), respectively. All the intensities are normalized to the maximum value; the blue asterisks are the measured data, and the dashed red lines are the best fits; the angle refers to the polarization direction of the pump laser. (**c**) Microscope images of the SH emission when pumping from P1 and P2, respectively, demonstrating the waveguiding and out-coupling of the SH signal.

doi:10.1038/lsa.2017.60

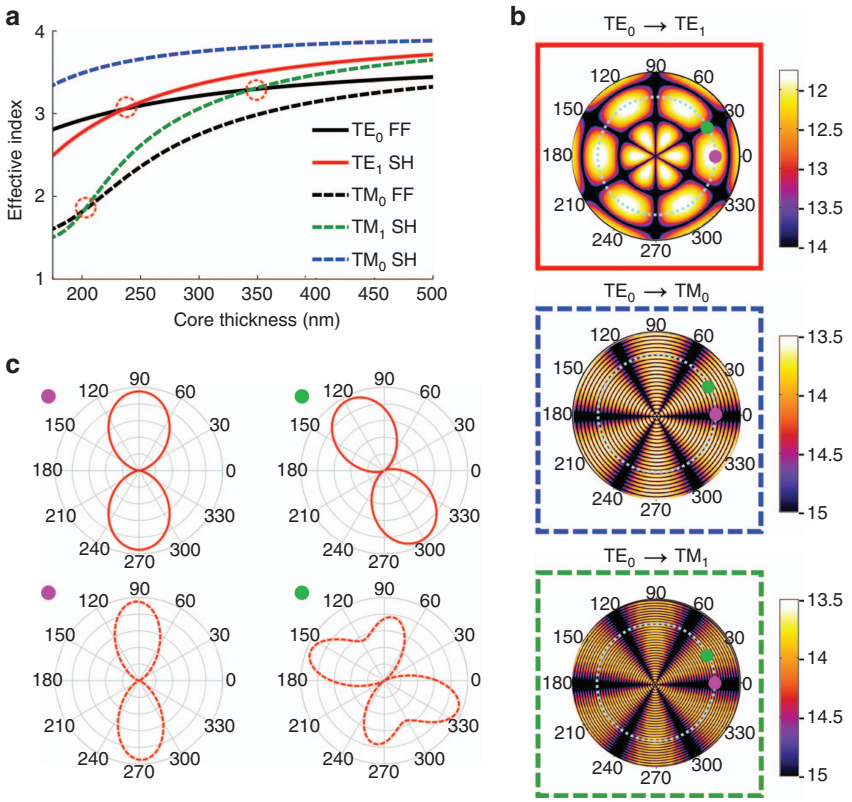

Figure 4 Numerical simulations. (**a**) Effective mode indices as a function of the core thickness for the TE- and TM-polarized guided modes at the FF and SH. The three red circles indicate the closest phase-matching points. (**b**) Color scale representation of the SH conversion efficiency (on a logarithmic scale) provided by the waveguide for the three dominant three wave-mixing processes, that is, $TE_0 \rightarrow TE_1$ (red solid box), $TE_0 \rightarrow TM_0$ (blue dashed box) and $TE_0 \rightarrow TM_1$ (green dashed box); the radial coordinate is the waveguide length (from 0 to 30 μm), and the azimuthal coordinate is the angle between the guided-mode propagation direction and the horizontal axis. The light-blue dotted circles refer to a waveguide length of 22 μm, approximately equal to the sample size. Purple and green dots correspond to points P1 and P2 of the experiment, respectively. (**c**) The total (solid red lines) and co-polarized component (dashed red lines) of the SH intensities as functions of the pump-laser polarization angle, φ (measured with respect to x axis), when focusing on positions P1 (purple dots) and P2 (green dots).

processes such as parametric amplification and generation as well as SPDC.

The internal conversion efficiency provided by the waveguide for the dominant nonlinear interaction, $TE_0 \rightarrow TE_1$, is given by

$$\eta_{TE_0 \rightarrow TE_1} = P_{SH}/P_{FF}^2 = \xi_{NL}^2 L_{wg}^2 \frac{\sin^2(\Delta\beta L_{wg}/2)}{(\Delta\beta L_{wg}/2)^2} \quad (1)$$

where P_{FF} is the power per unit length of the FF TE_0 mode at the waveguide input, P_{SH} is the SH power per unit length in the TE_1 mode measured at the waveguide output, L_{wg} is the interaction length along the waveguide, and $\Delta\beta = 2\beta^{FF} - \beta^{SH}$ is the wave vector mismatch. The nonlinear overlap factor in Equation (1) is defined as

$$\xi_{NL} = \chi^s_{MoSe_2} \sin(3\vartheta) \left(\frac{8\pi^2}{\varepsilon_0 c \lambda_{FF}^2 n_{SH} n_{FF}^2}\right)^{1/2} \frac{\left(E_{SH}^{*(TE_1)} E_{FF}^{2(TE_0)}\right)|_{z=z_{2D}}}{\left(\int_{wg} \left|E_{FF}^{(TE_0)}\right|^2 dz\right)\left(\int_{wg} \left|E_{SH}^{(TE_1)}\right|^2 dz\right)^{1/2}} \quad (2)$$

where $\chi^s_{MoSe_2} = 5.85 \times 10^{-18}\ m^2\ V^{-1}$ similar to other 2D crystals (WS_2)[15] is the quadratic nonlinear susceptibility of $MoSe_2$, ϑ is the angle formed by the guided-mode wave vector and the armchair direction of the $MoSe_2$ crystal, $\lambda_{FF} = 1550$ nm is the pump wavelength, $n_{FF,SH}$ are the effective refractive indices of the FF and SH modes, E_{FF} is the FF TE_0 mode profile, and E_{SH} is the SH TE_1 mode profile. In addition, z_{2D} indicates the vertical position of the $MoSe_2$ surface, that is, the interface between the silicon film and the air superstrate. The two normalization integrals at the denominator are calculated along the vertical direction (z axis). The expressions of the efficiency and the nonlinear overlap factor for the $TE_0 \rightarrow TM_0$ and the $TE_0 \rightarrow TM_1$ interactions can be written in a form analogous to Equations (1) and (2) by considering the appropriate effective refractive indices and mode profiles and by replacing $\sin(3\vartheta)$ with $\cos(3\vartheta)$ to properly take into account the 2D crystal anisotropy.

In Figure 4b, we show the calculated conversion efficiency for the three SHG processes discussed above as a function of the interaction length L_{wg} (varying from 0 to 30 μm) and the angle between the guided-mode wave vector and the horizontal axis. The color maps are on a logarithmic scale. The most coherent and efficient process is the $TE_0 \rightarrow TE_1$ interaction, whose maximum efficiency is about two orders of magnitudes larger than the efficiency of the other two processes. Due to the crystal anisotropy, when the FF TE_0 guided mode is excited near the point P1 (purple dots, corresponding to an interaction length of ~22 μm and $\vartheta = 30°$), the SHG is dominated by the $TE_0 \rightarrow TE_1$ interaction, and the other two interactions involving TM modes at the SH frequency are vanishing. By contrast, when the TE_0 FF guided mode is excited near the point P2 of the sample (green dots, corresponding to an interaction length of ~22 μm and $\vartheta = 0°$), the opposite response is obtained, that is, the $TE_0 \rightarrow TE_1$ interaction is

significantly suppressed, whereas the $TE_0 \rightarrow TM_0$ and $TE_0 \rightarrow TM_1$ interactions are maximized.

Next, we estimated the SH light intensity at the output grating as a function of the pump-laser polarization angle, φ, and compared these theoretical results to our experimental findings. The estimated total and co-polarized component of the SH light intensities versus pump-laser polarization angle are reported in the polar plots of Figure 4c for the two illumination positions investigated experimentally. The good agreement between theory and experiment, revealed by comparing Figures 4c and 3b, corroborates the idea that the waveguide indeed boosts the SHG of the nonlinear monolayer via the three nonlinear interactions mentioned above. More details of the calculation are presented in the Supplementary Information.

Finally, we calculated the maximal possible yield of the SHG that the $MoSe_2$-loaded silicon waveguide configuration could achieve under perfect phase-matching conditions. For example, the optimization of the $TE_0 \rightarrow TE_1$ process can be obtained via complete phase matching by changing the waveguide core thickness to 236 nm. Under the pumping conditions of the experiment, which included a spot size with a diameter of ~5 μm, and assuming diffraction-free propagation of the guided modes in the lateral (non-confined) dimension, a 22-μm-long waveguide could provide an SH signal 280-times stronger with respect to the case of direct pumping of the monolayer from the top at normal incidence, that is, in the absence of guided modes. This SH enhancement can be explained as follows: on one hand, the waveguide configuration amplifies the nonlinear interaction length by a factor L_{wg}/T_{MoSe_2}, where $T_{MoSe_2} = 0.65$ nm is the monolayer thickness; on the other hand, the overlap integral is limited by the extreme thinness of the nonlinear material. Notably, at phase matching, the enhancement factor would scale up quadratically with the nonlinear interaction length; for example, a 1-mm-long waveguide would boost the enhancement factor from 280 to 5.8×10^5.

CONCLUSION

In conclusion, we have demonstrated the integration of a TMDC monolayer on a silicon photonic platform for quadratic nonlinear optics applications. In particular, we have demonstrated 5-fold enhancement of the SHG from an atomically thin monolayer $MoSe_2$ through excitation of the 2D material by the evanescent field of the guided mode of a 220-nm planar waveguide. This enhancement is due to the increased interaction length, which proves that the length of the nonlinear interaction with light of 2D TMDCs, limited by monolayer thickness, could be overcome by integration with waveguide. Moreover, our calculations reveal how the mode conversion works in our system in different situations, and the results well match our experimental findings. The developed modeling predicts that the nonlinear signal could be further enhanced by optimizing the waveguide thickness to enable a full phase-matching condition. The results pave the way for many other nonlinear applications of 2D materials in optical domain, including parametric oscillations and efficient generation of entangled photon sources by SPDC. All such applications can be further advanced by possible electrical control of the nonlinear interactions in TMDCs[20].

CONFLICT OF INTEREST

The authors declare no conflict of interest.

ACKNOWLEDGEMENTS

H Chen acknowledges financial support from the China Scholarship Council for PhD scholarship no. 201206110047. We would like to acknowledge support from the Australian Research Council through Discovery Projects and participation in the Erasmus Mundus NANOPHI project, contract number 2013 5659/002-001. Device fabrication was supported by the ACT node of the Australian National Fabrication Facility.

1 Mak KF, Lee CG, Hone J, Shan J, Heinz TF. Atomically thin MoS_2: a new direct-gap semiconductor. *Phys Rev Lett* 2010; **105**: 136805.
2 Tongay S, Zhou J, Ataca C, Lo K, Matthews TS *et al.* Thermally driven crossover from indirect toward direct bandgap in 2D semiconductors: $MoSe_2$ versus MoS_2. *Nano Lett* 2012; **12**: 5576–5580.
3 Aharonovich I, Englund D, Toth M. Solid-state single-photon emitters. *Nat Photonics* 2016; **10**: 631–641.
4 Mak KF, He KL, Shan J, Heinz TF. Control of valley polarization in monolayer MoS_2 by optical helicity. *Nat Nanotechnol* 2012; **7**: 494–498.
5 Zeng HL, Dai JF, Yao W, Xiao D, Cui XD. Valley polarization in MoS_2 monolayers by optical pumping. *Nat Nanotechnol* 2012; **7**: 490–493.
6 Sallen G, Bouet L, Marie X, Wang G, Zhu CR *et al.* Robust optical emission polarization in MoS_2 monolayers through selective valley excitation. *Phys Rev B* 2012; **86**: 081301.
7 Jones AM, Yu HY, Ghimire NJ, Wu SF, Aivazian G *et al.* Optical generation of excitonic valley coherence in monolayer WSe_2. *Nat Nanotechnol* 2013; **8**: 634–638.
8 Li YL, Rao Y, Mak KF, You YM, Wang SY *et al.* Probing symmetry properties of few-layer MoS_2 and hBN by optical second-harmonic generation. *Nano Lett* 2013; **13**: 3329–3333.
9 Zeng HL, Liu GB, Dai JF, Yan YJ, Zhu BR *et al.* Optical signature of symmetry variations and spin-valley coupling in atomically thin tungsten dichalcogenides. *Sci Rep* 2013; **3**: 1608.
10 Kumar N, Najmaei S, Cui QN, Ceballos F, Ajayan PM *et al.* Second harmonic microscopy of monolayer MoS_2. *Phys Rev B* 2013; **87**: 161403.
11 Malard LM, Alencar TV, Barboza APM, Mak KF, Paula AMD. Observation of intense second harmonic generation from MoS_2 atomic crystals. *Phys Rev B* 2013; **87**: 201401.
12 Jones AM, Yu HY, Schaibley JR, Yan JQ, Mandrus DG *et al.* Excitonic luminescence upconversion in a two-dimensional semiconductor. *Nat Phys* 2016; **12**: 323–327.
13 Le CT, Clark DJ, Ullah F, Senthilkumar V, Jang JI *et al.* Nonlinear optical characteristics of monolayer $MoSe_2$. *Annal Phys* 2016; **528**: 551–559.
14 Yi F, Ren ML, Reed JC, Zhu H, Hou JC *et al.* Optomechanical enhancement of doubly resonant 2D optical nonlinearity. *Nano Lett* 2016; **16**: 1631–1636.
15 Janisch C, Wang YX, Ma D, Mehta N, Elías AL *et al.* Extraordinary second harmonic generation in tungsten disulfide monolayers. *Sci Rep* 2014; **4**: 5530.
16 Trolle ML, Tsao YC, Pedersen K, Pedersen TG. Observation of excitonic resonances in the second harmonic spectrum of MoS_2. *Phys Rev B* 2015; **92**: 161409.
17 Yin XB, Ye ZL, Chenet DA, Ye Y, O'Brien K *et al.* Edge nonlinear optics on a MoS_2 atomic monolayer. *Science* 2014; **344**: 488–490.
18 Mishina E, Sherstyuk N, Lavrov S, Sigov A, Mitioglu A *et al.* Observation of two polytypes of MoS_2 ultrathin layers studied by second harmonic generation microscopy and photoluminescence. *Appl Phys Lett* 2016; **106**: 131901.
19 Wang G, Marie X, Gerber I, Amand T, Lagarde D *et al.* Giant enhancement of the optical second-harmonic emission of WSe_2 monolayers by laser excitation at exciton resonances. *Phys Rev Lett* 2015; **114**: 097403.
20 Seyler KL, Schaibley JR, Gong P, Rivera P, Jones AM *et al.* Electrical control of second-harmonic generation in a WSe_2 monolayer transistor. *Nat Nanotechnol* 2015; **10**: 407–411.
21 Zeng JH, Yuan MH, Yuan WG, Dai QF, Fan HH *et al.* Enhanced second harmonic generation of MoS_2 layers on a thin gold film. *Nanoscale* 2015; **7**: 13547–13553.
22 Day JK, Chung MH, Lee YH, Menon VM. Microcavity enhanced second harmonic generation in 2D MoS_2. *Opt Mater Express* 2016; **6**: 2360–2365.
23 Fryett TK, Seyler KL, Zheng JJ, Liu CH, Xu XD *et al.* Silicon photonic crystal cavity enhanced second-harmonic generation from monolayer WSe_2. *2D Mater* 2017; **4**: 015031.
24 Leuthold J, Koos C, Freude W. Nonlinear silicon photonics. *Nat Photonics* 2010; **4**: 535–544.
25 Cazzanelli M, Bianco F, Borga E, Pucker G, Ghulinyan M *et al.* Second-harmonic generation in silicon waveguides strained by silicon nitride. *Nat Mater* 2012; **11**: 148–154.
26 Solntsev AS, Sukhorukov AA. Combined frequency conversion and pulse compression in nonlinear tapered waveguides. *Opt Lett* 2012; **37**: 446–448.
27 Liang D, Roelkens G, Baets R, Bowers JE. Hybrid integrated platforms for silicon photonics. *Materials* 2010; **3**: 1782–1802.
28 Majumdar A, Dodson CM, Fryett TK, Zhan A, Buckley S *et al.* Hybrid 2D material nanophotonics: a scalable platform for low-power nonlinear and quantum optics. *ACS Photonics* 2015; **2**: 1160–1166.
29 Gai X, Choi DY, Luther-Davies B. Negligible nonlinear absorption in hydrogenated amorphous silicon at 1.55 μm for ultra-fast nonlinear signal processing. *Opt Express* 2014; **22**: 9948–9958.
30 Benedikovic D, Cheben P, Schmid JH, Xu DX, Lamontagne B *et al.* Subwavelength index engineered surface grating coupler with sub-decibel efficiency for 220-nm silicon-on-insulator waveguides. *Opt Express* 2015; **23**: 22628–22635.
31 Xu DX, Schmid JH, Reed GT, Mashanovich GZ, Thomson DJ *et al.* Silicon photonic integration platform—have we found the sweet spot? *IEEE J Sel Top Quant Electron* 2014; **20**: 8100217.
32 Lockwood DJ, Pavesi L. *Silicon Photonics*. New York: Springer-verlag; 2004.

33 Vermeulen D, Selvaraja S, Verheyen P, Lepage G, Bogaerts W *et al.* High-efficiency fiber-to-chip grating couplers realized using an advanced CMOS-compatible silicon-on-insulator platform. *Opt Express* 2010; **18**: 18278–18283.
34 Masturzo SA, Yarrison-Rice JM, Jackson HE, Boyd JT. Grating couplers fabricated by electron-beam lithography for coupling free-space light into nanophotonic devices. *IEEE Trans Nanotechnol* 2007; **6**: 622–626.
35 Doerr CR, Buhl LL. Circular grating coupler for creating focused azimuthally and radially polarized beams. *Opt Lett* 2011; **36**: 1209–1211.
36 Tonndorf P, Schmidt R, Böttger P, Zhang X, Böttge J *et al.* Photoluminescence emission and Raman response of monolayer MoS_2, $MoSe_2$, and WSe_2. *Opt Express* 2013; **21**: 4908–4916.
37 Zhang Y, Chang TR, Zhou B, Cui YT, Yan H *et al.* Direct observation of the transition from indirect to direct bandgap in atomically thin epitaxial $MoSe_2$. *Nat Nanotechnol* 2014; **9**: 111–115.
38 Chen HT, Yang J, Rusak E, Straubel J, Guo R *et al.* Manipulation of photoluminescence of two-dimensional $MoSe_2$ by gold nanoantennas. *Sci Rep* 2016; **6**: 22296.
39 Haus HA, Reider GA. Enhancement of surface second harmonic generation with waveguides. *Appl Opt* 1987; **26**: 4576–4580.
40 Weismann M, Panoiu NC. Theoretical and computational analysis of second- and third-harmonic generation in periodically patterned graphene and transition-metal dichalcogenide monolayers. *Phys Rev B* 2016; **94**: 035435.
41 Yariv A. Coupled-mode theory for guided-wave optics. *IEEE J Quant Electron* 1973; **9**: 919–933.

This work is licensed under a Creative Commons Attribution-NonCommercial-ShareAlike 4.0 International License. The images or other third party material in this article are included in the article's Creative Commons license, unless indicated otherwise in the credit line; if the material is not included under the Creative Commons license, users will need to obtain permission from the license holder to reproduce the material. To view a copy of this license, visit http://creativecommons.org/licenses/by-nc-sa/4.0/

© The Author(s) 2017

Supplementary Information for this article can be found on the *Light: Science & Applications*' website (http://www.nature.com/lsa).